

INTERACTION BETWEEN SUPERNOVA REMNANT G22.7–0.2 AND THE AMBIENT MOLECULAR CLOUDS

YANG SU^{1,2}, JI YANG^{1,2}, XIN ZHOU^{1,2}, PING ZHOU³, AND YANG CHEN³

¹ Purple Mountain Observatory, Chinese Academy of Sciences, Nanjing 210008, China

² Key Laboratory of Radio Astronomy, Chinese Academy of Sciences, Nanjing 210008, China

³ Department of Astronomy, Nanjing University, 163 Xianlin Avenue, Nanjing 210023, China

Draft version June 22, 2021

ABSTRACT

We have carried out ¹²CO ($J=1-0$ and $2-1$), ¹³CO ($J=1-0$), and C¹⁸O ($J=1-0$) observations in the direction of the supernova remnant (SNR) G22.7–0.2. A filamentary molecular gas structure, which is likely part of a larger molecular complex with $V_{\text{LSR}} \sim 75-79 \text{ km s}^{-1}$, is detected and is found to surround the southern boundary of the remnant. In particular, the high-velocity wing ($77-110 \text{ km s}^{-1}$) in the ¹²CO ($J=1-0$ and $J=2-1$) emission shows convincing evidence of the interaction between SNR G22.7–0.2 and the $75-79 \text{ km s}^{-1}$ molecular clouds (MCs). Spectra with redshifted profiles, a signature of shocked molecular gas, are seen in the southeastern boundary of the remnant. The association between the remnant and the 77 km s^{-1} MCs places the remnant at the near distance of $4.4 \pm 0.4 \text{ kpc}$, which agrees with a location on the Scutum–Crux arm. We suggest that SNR G22.7–0.2, SNR W41, and H II region G022.760–0.485 are at the same distance and are associated with GMC G23.0–0.4.

Subject headings: ISM: individual (G22.7–0.2) – ISM: molecules – supernova remnants

1. INTRODUCTION

Massive stars form from molecular clouds (MCs) and they interact with their ambient interstellar medium (ISM). Mass and energy deposition from the massive stars into the surrounding ISM occurs via strong ultraviolet radiation, powerful stellar winds, and finally, violent supernova explosions. When these blast waves hit the nearby MCs, the shocks will compress, heat, accelerate, and even dissociate the molecular gas, which leads to a wide variety of observable effects. The interplay between the shock and the molecular gas may trigger star formation in the nearby giant molecular cloud (GMC). A shock interaction with MCs can also generate γ -rays as a result of a neutral pion decay after a p - p collision (hadronic interaction), which may exhibit observable very high energy (VHE) emissions. In all of the study field, the molecular emission is a useful tool to investigate the nature of shock–MC interactions (see a recently view in Chen et al. 2014).

Supernova remnant (SNR) G22.7–0.2, with a diameter of $26'$, is listed in the catalog of Green (1991). The remnant is located in a complex field with multiple H II regions and an adjacent SNR G23.3–0.3 (W41) (see Figures 11 and 12 in Messineo et al. 2010) that has been studied less. SNR G22.7–0.2 shows a faint shell structure in the radio emission and it displays a concave structure on the southern part of the shell. There are numerous mid-infrared filaments evident at $5.8-8 \mu\text{m}$ in coincidence with the radio shell of the remnant, which was suspected as a possible region of SNR–MC interaction (Reach et al. 2006). Helfand et al. (2006) identified the G22.7–0.2's southern object G22.7583–0.4917 as a SNR candidate with $5'0$ diameter, while Thompson et al. (2006) suggested that G22.76–0.49 is probably an H II region. Including the H II regions or SNR candidates in the field of view (FOV) of SNR G22.7–0.2 (Helfand et al.

2006; Anderson et al. 2014), a VHE source, HESS J1832–093, is lying on the western edge of SNR G22.7–0.2, but its origin remains undetermined (Laffon et al. 2013).

The study of SNR G22.7–0.2 is motivated by the possible relationship between the multiple objects and the remnant in the complex region. We performed new millimeter CO ($J=1-0$) observations (covering about 1 deg^2) toward the remnant to investigate the overall MC distribution surrounding the complex region. Very wide $77-110 \text{ km s}^{-1}$ line broadenings are seen in the spectra of ¹²CO ($J=1-0$ and $J=2-1$) in the southeastern boundary of the remnant; this represents evidence for shock–MC interactions. We suggest that the $V_{\text{LSR}} \sim 75-79 \text{ km s}^{-1}$ MCs are physically associated with the remnant because of the spatial and kinematic features. We also explore the relationship between the SNR G22.7–0.2 and the overlapping H II regions.

The paper is structured as follows. In Section 2, we show the CO observations and the data reduction. In Sections 3 and 4, we describe the main results and the physical discussion, respectively. A brief summary is given in Section 5.

2. OBSERVATIONS AND DATA REDUCTION

The observations toward SNR G22.7–0.2 were made simultaneously in the ¹²CO ($J=1-0$) line (at 115.271 GHz), the ¹³CO ($J=1-0$) line (110.201 GHz), and the C¹⁸O ($J=1-0$) line (109.782 GHz) during 2013 March and April using the 13.7 m millimeter-wavelength telescope of the Purple Mountain Observatory at Delingha in China. It is a part of the Milky Way Imaging Scroll Painting (MWISP) project for investigating the nature of the molecular gas along the northern Galactic Plane. We used a new 3×3 pixel Superconducting Spectroscopic Array Receiver as the front end, which was made with Superconductor–Insulator–Superconductor (SIS) mixers using the sideband sepa-

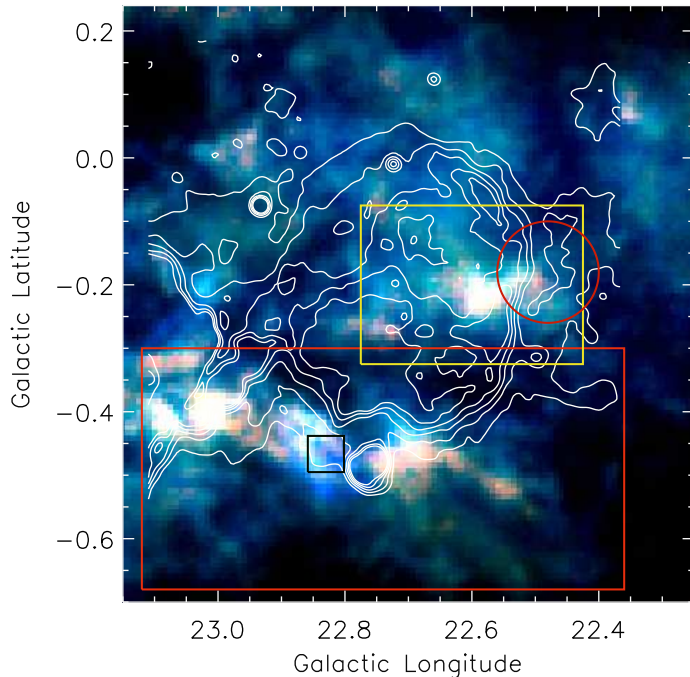


FIG. 1.— ^{12}CO ($J=1-0$; blue), ^{13}CO ($J=1-0$; green), and C^{18}O ($J=1-0$; red) intensity maps in the $71-86 \text{ km s}^{-1}$ interval with a linear scale of SNR G22.7–0.2 overlaid with the VGPS 1.4 GHz radio continuum emission contours. The black box indicates the region from which the spectra of the shocked gas are extracted (see Figure 3). The red rectangle and the yellow rectangle show the region of GMC G23.0–0.4W and GMC G22.6–0.2, respectively. The red circle shows the location of HESS J1832–093 (Laffon et al. 2013). SNR W41 (G23.3–0.3) is located to the left of SNR G22.7–0.2.

rating scheme (Shan et al. 2012; Zuo et al. 2011). An instantaneous bandwidth of 1 GHz was used as the backend. Each spectrometer provided 16,384 channels, resulting in a spectral resolution of 61 kHz, equivalent to a velocity resolution of about 0.16 km s^{-1} for ^{12}CO and 0.17 km s^{-1} for ^{13}CO and C^{18}O . The half-power beam width (HPBW) of the telescope was about $50''$, and the pointing accuracy of the telescope was greater than $4''$ in the observing epoch. We used the on-the-fly observing technique to map the $0^\circ 9 \times 0^\circ 9$ area centered at ($l=22^\circ 75$, $b=-0^\circ 25$) with a scan speed of $50'' \text{ s}^{-1}$ and a step of $15''$ along the Galactic longitude and latitude. The mean rms noise level of the brightness temperature (T_{R}) was about 0.5 K for ^{12}CO and 0.3 K for ^{13}CO and C^{18}O . All of the CO data used in this study are expressed in brightness temperature. Here we adopt the main beam efficiency $\eta_{\text{mb}} = 0.44$ for ^{12}CO and 0.48 for ^{13}CO and C^{18}O ($T_{\text{R}} = T_{\text{A}} / (f_{\text{b}} \times \eta_{\text{mb}})$, assuming a beam filling factor of $f_{\text{b}} \sim 1$).

We also used the ^{12}CO ($J=2-1$) line (at 230.538 GHz), which was observed during 2010 January and February using the 3 m submillimeter telescope at the Kölner Observatory for Submillimeter Astronomy (KOSMA) in Switzerland. An SIS receiver and a medium-resolution acoustic-optical spectrometer (AOS) spectrometer were used. The map of 0.33 deg^2 was centered at ($18^{\text{h}}33^{\text{m}}19^{\text{s}}$, $-09^{\circ}10'42''$) with a grid spacing of $1'$. The HPBW of the telescope was $130''$ and the main beam efficiency was about 0.54 during our observation.

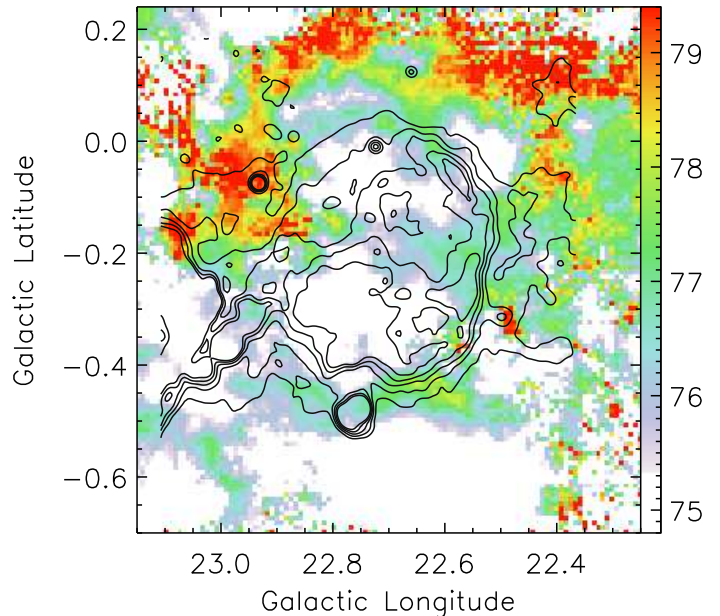


FIG. 2.— Intensity-weighted mean velocity (first moment) map of the ^{13}CO ($J=1-0$) emission on the interval of $70-81 \text{ km s}^{-1}$ of SNR G22.7–0.2 overlaid with the VGPS 1.4 GHz radio continuum emission contours. The color scheme is adjusted to highlight the velocity range of $75-79 \text{ km s}^{-1}$.

The AOS bandwidth and velocity resolution were about 300 MHz and 0.2 km s^{-1} , respectively.

All of the CO data were reduced using the GILDAS/CLASS package developed by IRAM¹. Finally, the baseline-corrected spectra of CO ($J=1-0$) were converted to three-dimensional cube data with a grid spacing of $30''$ and a velocity channel separation of 0.5 km s^{-1} for subsequent analysis. The spectra of CO ($J=2-1$) were converted to $1' \times 1' \times 0.5 \text{ km s}^{-1}$ cube data.

The VLA Galactic Plane Survey (VGPS, Stil et al. 2006) radio continuum emissions were also used for comparison.

3. RESULTS

3.1. MC Distribution Toward SNR G22.7–0.2

In the FOV of SNR G22.7–0.2, the ^{12}CO ($J=1-0$) is in a broad velocity range between 0 and 130 km s^{-1} , characterized by multiple peaks because the remnant is near the inner Galaxy. After checking the CO emission intensity maps channel by channel, we found a morphological correlation between the $71-86 \text{ km s}^{-1}$ MCs and SNR G22.7–0.2.

The $71-86 \text{ km s}^{-1}$ MCs were also called the molecular cloud complex [23,78] based on 1.2m CO survey (Dame et al. 1986). On the other hand, Messineo et al. (2014) identified this GMC as G23.3–0.3 at a distance of 4–5 kpc (Albert et al. 2006). Based on our new CO observations (see Section 2), we identified the molecular cloud complex as GMC G23.0–0.4 ($V_{\text{LSR}} \sim 77 \text{ km s}^{-1}$). The GMC G23.0–0.4 centered at ($l=23^\circ 0$, $b=-0^\circ 4$) covers about $1^\circ 1 \times 0^\circ 4$ area in ^{13}CO emission and it generally shows the filamentary structure.

Figure 1 shows a portion of GMC G23.0–0.4 that cov-

¹ <http://www.iram.fr/IRAMFR/GILDAS>

TABLE 1
 PROPERTIES OF GMCs

GMC	$T_{\text{ex}}(\text{CO})$ (K)	$\tau(^{13}\text{CO})$	Size ($'\times'$)	$V_{\text{LSR}}(\text{peak})$ (km s^{-1})	Column Density ^a (10^{22}cm^{-2})	Mass ^{a,b} ($10^5 M_{\odot}$)	Density ^{a,b,c} (cm^{-3})
G22.6–0.2	18	0.27	14 \times 10	76.4	2.7/2.3	$1.4d_{4.4}^2/1.2d_{4.4}^2$	$680d_{4.4}^{-1}/580d_{4.4}^{-1}$
G23.0–0.4W	23	0.12	40 \times 22	76.6	2.6/1.9	$8.2d_{4.4}^2/5.7d_{4.4}^2$	$330d_{4.4}^{-1}/240d_{4.4}^{-1}$

NOTE. — ^a See text for the two methods (LTE/X-factor) used for the calculation. ^b Parameter $d_{4.4}$ is the distance to the cloud in units of 4.4 kpc. ^c Assuming a depth of 10' for GMC G22.6–0.2 and 20' for GMC G23.0–0.4W along the line of sight.

Glon: 22.833333
 Glat: -0.46666667

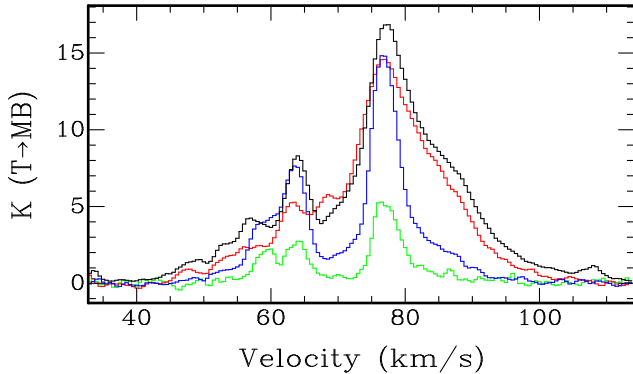


FIG. 3.— $^{12}\text{CO}(J=1-0)$; black), $^{13}\text{CO}(J=1-0)$; blue, multiplied by a factor of three), $\text{C}^{18}\text{O}(J=1-0)$; green, multiplied by a factor of six), and $^{12}\text{CO}(J=2-1)$; red) spectra of the shocked gas extracted from the region indicated in Figure 1 (black box).

ers the SNR G22.7–0.2. The composite image displays the intensity map of the CO lines integrated in the 71–86 km s^{-1} interval ($^{12}\text{CO } J=1-0$ in blue, $^{13}\text{CO } J=1-0$ in green, and $\text{C}^{18}\text{O } J=1-0$ in red). The brightest portions of the three lines are found in the region of the west part of the GMC G23.0–0.4 (about $1^{\circ}1\times 0^{\circ}4$ in size) and GMC G22.6–0.2 (about $0^{\circ}3\times 0^{\circ}2$ in size). Hereafter, we regard the west part of GMC G23.0–0.4 as G23.0–0.4W. In GMC G23.0–0.4W (Figure 1), the CO emission shows a filamentary structure that nicely surrounds and folds the southern region of SNR G22.7–0.2. The GMC G22.6–0.2 is located in the west of the remnant (see the yellow rectangle in Figure 1) along with HESS J1832-093 (see the red circle in Figure 1). Several relatively faint filamentary structures are also seen around the northern part of the remnant. To investigate the detailed structures of the MCs in the vicinity of SNR G22.7–0.2, we made an intensity-weighted velocity (the first moment) map of ^{13}CO emission in the velocity range of 70–81 km s^{-1} (see Figure 2). In Figure 2, we can see the same filamentary structure in the GMC G23.0–0.4W. The filament surrounds SNR G22.7–0.2 and has a velocity of $\sim 76\text{--}78 \text{ km s}^{-1}$. In the northern border, the higher velocity ($V_{\text{LSR}} \sim 79 \text{ km s}^{-1}$) of the molecular gas inherent to the SNR could be contaminated by other clouds at 80–90 km s^{-1} . Similar high velocity gas is visible roughly in the top panel of Figure 11 of Messineo et al. (2014). The $^{13}\text{CO}(J=1-0)$ velocity coded image of SNR G22.7–0.2 generally seems to show a cavity structure.

We show the physical properties of the GMCs G23.0–0.4W and G22.6–0.2 in Table 1. Here two methods have been used in the derivation of the column den-

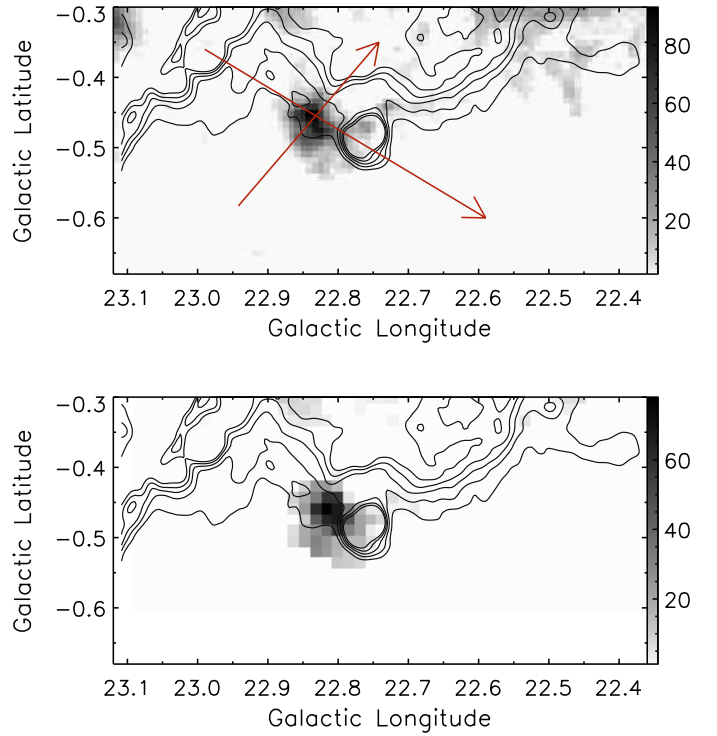


FIG. 4.— Top: the $^{12}\text{CO}(J=1-0)$ intensity map in the 86–99 km s^{-1} interval displayed the linear scale and overlaid with the VGPS 1.4 GHz radio continuum emission contours. The red arrows show the direction of the PV diagrams (see Figure 5). Bottom: $^{12}\text{CO}(J=2-1)$ intensity maps in the 86–99 km s^{-1} interval.

sities and the masses of the GMCs. In the first method, on the assumption of local thermodynamic equilibrium (LTE) and the $^{12}\text{CO}(J=1-0)$ line being optically thick, we can derive the excitation temperature from the peak radiation temperature of the $^{12}\text{CO}(J=1-0)$. The $^{13}\text{CO}(J=1-0)$ emission is optically thin and the ^{13}CO column density is converted to the H_2 column density using $N(\text{H}_2)/N(^{13}\text{CO}) \approx 7 \times 10^5$ (Frerking et al. 1982). In the second method, the H_2 column density is estimated by adopting the mean CO-to- H_2 mass conversion factor $1.8 \times 10^{20} \text{ cm}^{-2}\text{K}^{-1}\text{km}^{-1}\text{s}$ (Dame et al. 2001). In the estimate of the mass of the GMCs, a mean molecular weight per H_2 molecule of 2.76 has been adopted. The distance of the GMCs was adopted as 4.4 kpc (see Section 4.1).

We found that the derived physical parameters of the LTE method are similar to that of the X-factor method (Table 1). On the other hand, the mean optical depth of the $^{13}\text{CO}(J=1-0)$ emission of GMC G23.0–0.4W is a half of that of GMC G22.6–0.2.

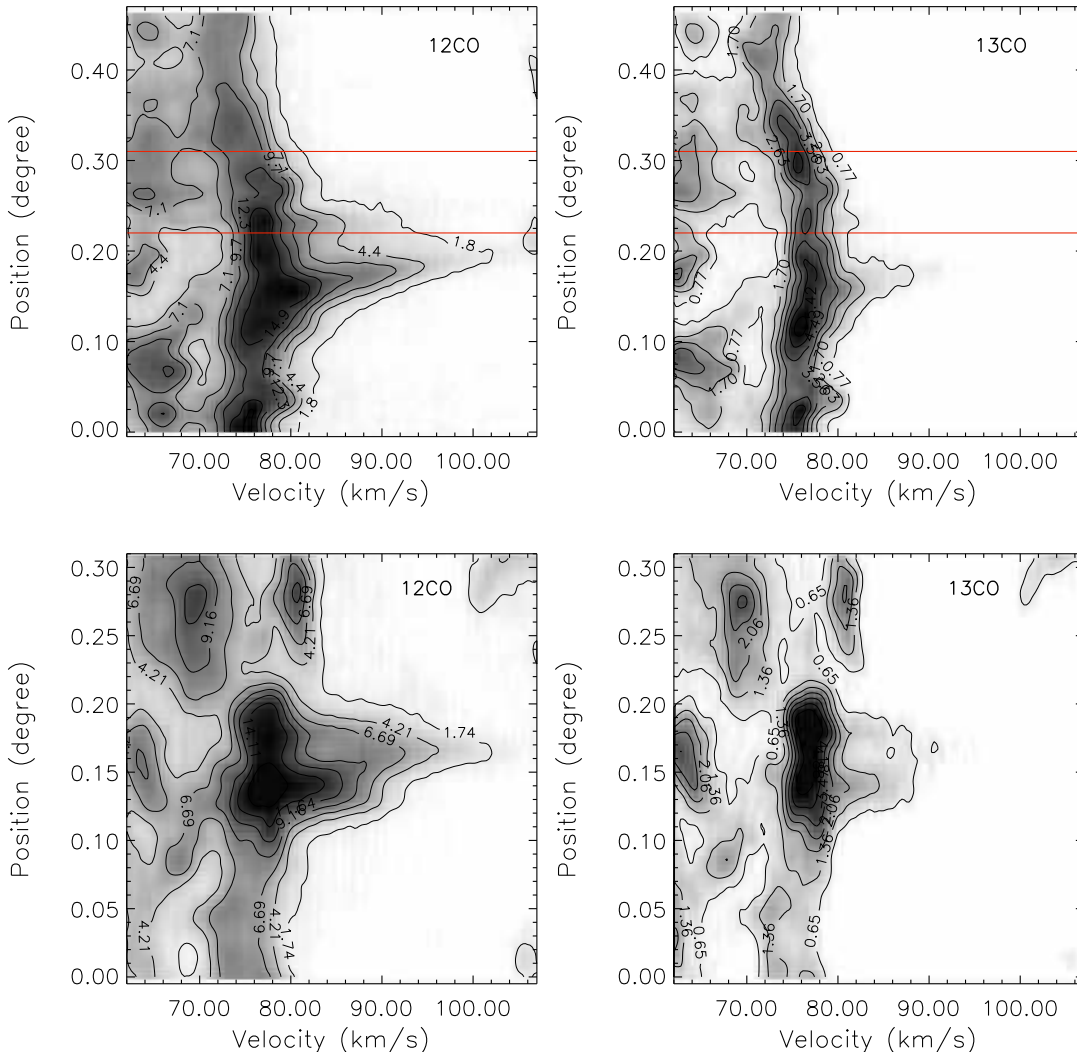


FIG. 5.— PV diagrams of the ^{12}CO ($J=1-0$) and ^{13}CO ($J=1-0$) emission toward the shocked gas. The position is measured along the long arrow ($(l=22^\circ 990, b=-0^\circ 360)$ to $(l=22^\circ 590, b=-0^\circ 590)$, upper panels) and the short arrow ($(l=22^\circ 942, b=-0^\circ 583)$ to $(l=22^\circ 742, b=-0^\circ 350)$, lower panels) with a width of $1.5'$ (see Figure 4). The red lines in the upper panels mark the spatial region of H II region G22.76–0.485 (ID 06 in Table 3).

3.2. Shocked Molecular Gas in the Remnant

To search for the kinematic evidence for the interaction between SNR G22.7–0.2 and the ambient MCs, we analyzed the spectra of the ^{12}CO ($J=1-0$ and $J=2-1$) emission of the remnant in detail. The spectra of the ^{13}CO ($J=1-0$) were also used for comparison, considering that the ^{13}CO line is more optically thin than the ^{12}CO lines and thus can be used to show the relatively undisturbed component. We found the clear line broadening structure of the ^{12}CO emission in the southeastern region of the remnant, which extends from the peak velocity of $\sim 77 \text{ km s}^{-1}$ to $\sim 110 \text{ km s}^{-1}$. The redshifted profile indicates that the molecular gas of the 77 km s^{-1} MC is mainly located behind the expanding SNR. The spectra are shown in Figure 3 and the spectral extraction region is indicated by the black box in Figure 1. The ^{12}CO ($J=1-0$ and $J=2-1$) line broadenings provide kinematic evidence for the interaction between SNR G22.7–0.2 and the ambient molecular gas with a system velocity of $\sim 77 \text{ km s}^{-1}$. Figure 4 displays the intensity

maps of the shocked gas in the $86\text{--}99 \text{ km s}^{-1}$ interval. The distribution of the shocked gas seems to extend along the southeastern radio border of SNR G22.7–0.2.

We did not find the broadening profile of the ^{12}CO emission in the region of GMC G22.6–0.2, although it has a similar velocity to that of the southern cloud in GMC G23.0–0.4W and it is projectively located inside the remnant. There may be two possible reasons to explain this. First, the GMC G22.6–0.2 is not actually in physical contact with SNR G22.7–0.2, but is instead in the foreground or background of the remnant. Second, the SNR’s shock is interacting with the molecular gas of the GMC G22.6–0.2. In this case, the broadened lines are probably contaminated by other velocity components between 70 km s^{-1} and 90 km s^{-1} . This limited our investigation for the SNR–MC interaction in CO emission. Other observations are needed to clarify the issue.

Figure 5 shows the position–velocity (PV) diagrams of the shocked gas along and perpendicular to the southeastern radio boundary of SNR G22.7–0.2 (see the red

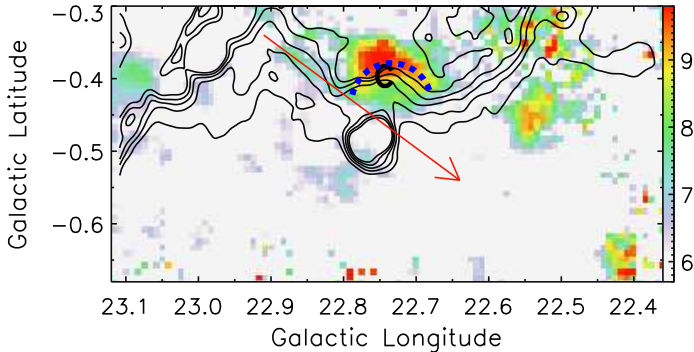


FIG. 6.— Intensity-weighted mean velocity dispersion (second moment) map of the ^{13}CO ($J=1-0$) emission in the interval of $70-81 \text{ km s}^{-1}$ of the molecular gas in GMC G23.0–0.4W, overlaid with the VGPS 1.4 GHz radio continuum emission contours. The color scheme is adjusted to highlight the enhancement of the velocity dispersion. The red arrow indicates the direction of the PV diagrams (see Figure 7) and the blue dotted line indicates the concave structure. The character “C” indicates the location of the stellar cluster GLIMPSE9 (Messineo et al. 2010).

arrows in Figure 4). We can discern the quiescent component in the $70-81 \text{ km s}^{-1}$ interval (see the ^{13}CO PV diagrams in the right panels) and the shocked component in the $83-106 \text{ km s}^{-1}$ interval (see the ^{12}CO PV diagrams in the left panels). The highest velocity of the shocked gas as revealed by the ^{12}CO PV diagrams is extended to $\sim 110 \text{ km s}^{-1}$, indicative of $\sim 30 \text{ km s}^{-1}$ shock velocity at least. The value of the broadening velocity is comparable to that of SNR W44 ($>25 \text{ km s}^{-1}$; Seta et al. 2004) and SNR IC 443 ($10-100 \text{ km s}^{-1}$; Snell et al. 2005). On the other hand, the value of the broadening velocity of SNR G22.7–0.2 is larger than that found in other SNR–MC interaction systems (several kilometers per second for SNR Kes 75 and SNR 3C 396; Su et al. 2009, 2011).

We also made an intensity-weighted velocity dispersion (the second moment) map of the ^{13}CO emission in the velocity range of $70-81 \text{ km s}^{-1}$ toward the molecular gas in GMC G23.0–0.4W (see Figure 6). This roughly shows the velocity dispersion in the given velocity range of $70-81 \text{ km s}^{-1}$: the higher the velocity dispersion, the greater the range of velocities. Some interesting structures are found to be located in the south of the remnant. In Figure 6, a filamentary structure (the red arrow) and a concave structure (the blue dotted line) seem to be associated with the remnant. The arrow is roughly located at the inner border of the SNR shell as seen in Figures 1 and 2. The ^{12}CO PV diagram of the filament also shows the line broadening structure (see the $84-90 \text{ km s}^{-1}$ emission in the left panel of Figure 7) compared to the ^{13}CO PV diagram (right panel of Figure 7), which is likely due to the shock–MC interaction in the region. We will discuss the possible origin of the concave structure in Section 4.2.

The CO component in the velocity of $\sim 60-70 \text{ km s}^{-1}$ limited the investigation for the blueshifted wing of the shocked gas. However, the enhancement of the ^{12}CO ($J=2-1$) in the interval of $68-74 \text{ km s}^{-1}$ probably indicates the shock–MC interaction (see Figure 3). More observations are needed to clarify the characteristics of the shocked gas in the region.

Weak ^{13}CO ($J=1-0$) emission has been detected from the high-velocity wings in the region of the shocked gas (see Figures 3 and 5), which probably indicates that the ^{12}CO ($J=1-0$) line wings are not optically thin. Coincidentally, SNR IC 443, another SNR–MC system, also displays very weak wings of the ^{13}CO ($J=1-0$) line in the velocity interval of -50 to -10 km s^{-1} toward the shocked gas of the clump B (see Figure 15 in Zhang et al. 2010). It shows that the ^{12}CO emission of the broadening for shocked gas probably has a median optical depth for some cases.

If the excitation temperatures and the beam filling factors of the ^{12}CO ($J=1-0$) and ^{13}CO ($J=1-0$) lines are equal, the average optical depth of the shocked gas can be estimated from the ratio of the integrated intensity over the high-velocity emission for $^{12}\text{CO}/^{13}\text{CO}$ (Snell et al. 1984). The integrated intensity ratio value is about 20.9 for a $5' \times 5'$ shocked region centered at ($l=22^\circ 833, b=-0^\circ 467$). Assuming the optical depth of ^{13}CO ($J=1-0$) emission $\tau(13) \ll 1$ in the line wing and the isotopic ratio $^{12}\text{C}/^{13}\text{C} = \tau(12)/\tau(13) = 41$ (Milam et al. 2005), we get the optical depth of $\tau(12) \sim 1.6$ for the shocked high velocity ^{12}CO ($J=1-0$) gas. We note that the optical depth estimated for the shocked gas is close to that of the stellar cluster GLIMPSE9 in K_S band (Messineo et al. 2010). The column density of the shocked gas in the interval of $83-106 \text{ km s}^{-1}$ (Figure 5) can be estimated as $2.4 \times 10^{21} \text{ cm}^{-2}$. The mean density of the shocked gas is about $120 d_{4.4}^{-1} \text{ cm}^{-3}$ assuming the depth of $5'$ along the line of sight, where $d_{4.4} = d/(4.4 \text{ kpc})$ is the distance scaled with 4.4 kpc (see Section 4.1). In the above calculation, a uniform excitation temperature ($T_{\text{ex}}=23 \text{ K}$, Table 1) and a conversion factor $N(\text{H}_2)/N(^{12}\text{CO}) \approx 1 \times 10^4$ (Herbst & Leung 1989) are assumed. Therefore, the mass, momentum, and energy of the high velocity shocked gas are estimated to be $2.2 d_{4.4}^2 \times 10^3 M_\odot$, $3.3 d_{4.4}^2 \times 10^4 M_\odot \text{ km s}^{-1}$, and $5.0 d_{4.4}^2 \times 10^{48} \text{ erg}$, respectively. These values should be regarded as lower limits since it is very likely that the excitation temperature is $T_{\text{ex}}(\text{CO wing}) \geq 23 \text{ K}$ at the shock-heated region and that the optical depth of ^{12}CO ($J=1-0$) emission is $\tau(12) \geq 1.6$ for the region of the high column density. Additionally, the low-velocity component of the shocked gas is not accounted for because of the contamination of the line center emission.

4. DISCUSSION

4.1. Association of SNR G22.7–0.2 with the 77 km s^{-1} MCs and the Distance to the Remnant

In Section 3, we showed spatial and kinematic evidence for the association between SNR G22.7–0.2 and the $V_{\text{LSR}} \sim 77 \text{ km s}^{-1}$ MCs. First, the molecular gas in GMC G23.0–0.4W at a radial velocity of $71-86 \text{ km s}^{-1}$ is found to surround the southern radio shell of the remnant (Figures 1 and 2). The map of the ^{13}CO velocity distribution seems to display a cavity structure in which SNR G22.7–0.2 is embedded (Figure 2). Second, the $83-110 \text{ km s}^{-1}$ red wing of the ^{12}CO ($J=1-0$ and $J=2-1$) emission is found in a region of GMC G23.0–0.4W ($l=22^\circ 833, b=-0^\circ 467$), providing convincing kinematic evidence for the SNR–MC interaction (Figures 3 and 5).

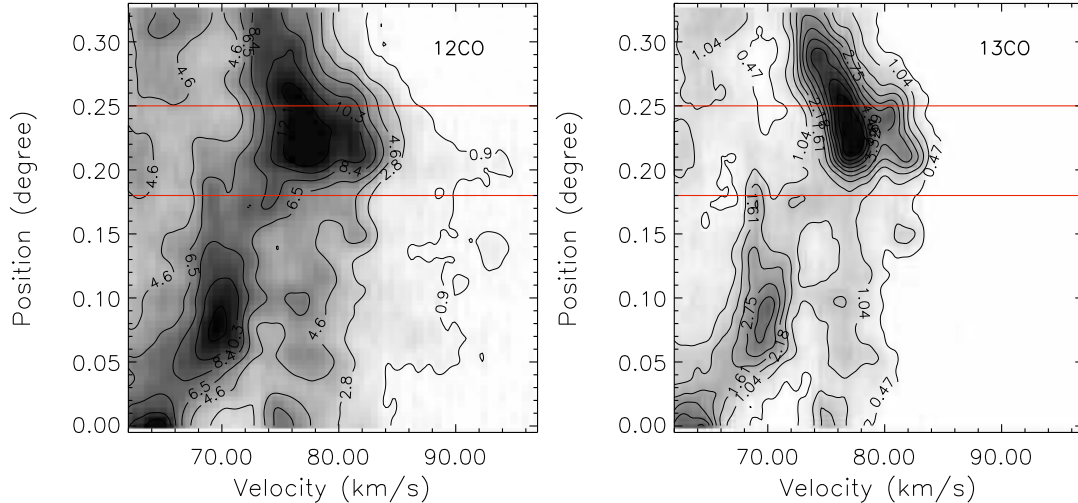


FIG. 7.— PV diagrams of the ^{12}CO ($J=1-0$) and ^{13}CO ($J=1-0$) emission along the molecular gas slice, which is located along the southeastern bright radio shell of the remnant. The position is measured along the arrow ($(l=22^\circ 910, b=-0^\circ 340)$ to $(l=22^\circ 640, b=-0^\circ 520)$, see Figure 6) with a width of $1'.5$. The red lines mark the spatial region of H II region G22.76–0.485 (ID 06 in Table 3).

TABLE 2
DUST-CONTINUUM-IDENTIFIED MC CLUMPS TOWARD SNR
G22.7–0.2

ID	l (deg)	b (deg)	V_{LSR}^a (km s^{-1})	Distance ^a (kpc)
a	22.474	−0.223	75.9	$4.70^{+0.36}_{-0.36}$
b	22.494	−0.207	75.8	$4.58^{+0.26}_{-0.28}$
c	22.504	−0.197	76.8	$4.64^{+0.28}_{-0.32}$
d	22.534	−0.193	75.6	$4.66^{+0.32}_{-0.34}$
e	22.694	−0.454	77.9	$4.70^{+0.26}_{-0.30}$
f	22.836	−0.418	73.4	$4.50^{+0.30}_{-0.34}$
g	22.870	−0.408	75.4	$4.54^{+0.34}_{-0.34}$
h	22.878	−0.434	76.8	$4.44^{+0.30}_{-0.30}$
i	22.906	−0.466	76.8	$4.60^{+0.32}_{-0.34}$

NOTE. — ^a See Section 3 and Table 3 in Ellsworth-Bowers et al. (2013).

The ^{12}CO PV diagram of a filament along the southeastern radio shell ($(l=22^\circ 850, b=-0^\circ 384)$, see the red arrow in Figure 6) also displays the broadening structure, which further supports the interaction between the remnant and the 77 km s^{-1} MCs (the left panel in Figure 7).

The association of SNR G22.7–0.2 with the MCs at the systemic velocity, $\sim 77 \text{ km s}^{-1}$, enables us to place the SNR at a near kinematic distance of $4.4 \pm 0.4 \text{ kpc}$ by using the Galactic rotation curve model of Reid et al. (2014). We also exclude the far distance of the 77 km s^{-1} MCs based on the H I self-absorption method (Roman-Duval et al. 2009). The $4.4 \pm 0.4 \text{ kpc}$ kinematic distance with a system velocity of $\sim 77 \text{ km s}^{-1}$, roughly places the remnant at the near side of the Scutum–Crux arm (see the distance of the Galactic arm in Taylor & Cordes 1993; Sewilo et al. 2004). It is also consistent with the distance of the dense clumps in the GMC with velocity of $\sim 77 \text{ km s}^{-1}$ (Table 2), which is estimated for dust-continuum-identified MC clumps from the Bolocam Galactic Plane Survey in the inner Galaxy (Ellsworth-Bowers et al. 2013). These MC clumps are

probably the cradle of massive star formation in the GMC with a velocity of $\sim 77 \text{ km s}^{-1}$. We note that the distance of SNR G22.7–0.2 is close to that of the nearby SNR W41 (see the radio contours in the east of Figure 1). Leahy & Tian (2008) estimated the kinematic distance of 3.9–4.5 kpc for SNR W41 based on the H I and ^{13}CO data. Recently, Frail et al. (2013) report on the discovery of 1720 MHz OH line emission of the radio continuum of SNR W41 with the radial velocity of 74 km s^{-1} , which is strong evidence for a SNR–MC interaction system. The radial velocity of the OH emission coincides with the system velocity of the east part of GMC G23.0–0.4, indicative of the interaction between SNR W41 and the GMC. Moreover, the east part of GMC G23.0–0.4 with $V_{\text{LSR}} \sim 77 \text{ km s}^{-1}$ extends toward SNR W41 and it covers the projected area of the remnant. The east part of GMC G23.0–0.4 is probably partly responsible for the bright VHE emission of HESS J1834–087 (see Section 4.3). Since SNRs G22.7–0.2 and W41 are both interacting with the GMC G23.0–0.4, the two SNRs are at a similar distance.

The radius of SNR G22.7–0.2 is about $18d_{4.4} \text{ pc}$ and no extended X-ray emission has been detected up to now. Assuming the $\sim 100 \text{ km s}^{-1}$ expansion velocity of the shock in the radiative phase, the age of SNR G22.7–0.2 is about several tens of thousands of years. Adopting the SNR’s radius of $\sim 14'$, the solid angle of the shocked gas is about 0.1 sr in the southeastern boundary of the remnant. Thus we estimated the kinetic energy of the remnant to be at least $\sim 6.3d_{4.4}^2 \times 10^{50} \text{ erg}$, which is consistent with the typical kinetic energy release of 10^{51} erg for a SNR.

4.2. Relationship Between the SNR and the Overlapping Star-forming Regions

There are multiple H II regions in the FOV of SNR G22.7–0.2. We list the physical parameters of these H II regions in Table 3. Most of the H II regions seem to be associated with the 70–81 km s^{-1} MCs, e.g., GMC G23.0–0.4W (see Figure 8). The H II region G022.760–0.485 with a systemic velocity of

TABLE 3
OVERLAPPING H II REGIONS TOWARD SNR G22.7–0.2

ID	Name	l (deg)	b (deg)	Radius (arcmin)	V_{LSR} (km s^{-1})	Ref. ^a
01	G022.398+0.083	22.398	+0.083	...	87.8	3
02	G022.724–0.010	22.724	–0.010	0.7	38.9	1,2
03	G022.730–0.239	22.730	–0.239	1.0	71.1/113.7	1,2
04	G022.739–0.303	22.739	–0.303	...	69.3/112.1	1
05	G022.755–0.246	22.755	–0.246	1.2	70.2/106.7	1,2
06 ^b	G022.760–0.485	22.760	–0.485	2.6	74.8	2,3,5
07	G022.780–0.383	22.780	–0.383	1.7	70.0	1,2
08	G022.935–0.072	22.935	–0.072	...	71.2	4
09	G022.947–0.315	22.947	–0.315	0.7	70.9	2,3
10 ^c	G022.982–0.356	22.982	–0.356	2.5	74.1	2,3
11	G022.986–0.149	22.986	–0.149	1.9	76.6/100.2	1,2
12	G023.029–0.405	23.029	–0.405	2.5	76.0	1
13	G023.067–0.367	23.067	–0.367	...	82.7	3
14	G023.072–0.248	23.072	–0.248	...	89.6	3

NOTE. — ^a (1) Anderson et al. 2011; (2) Anderson et al. 2014; (3) Lockman 1989; (4) Lockman et al. 1996; (5) Thompson et al. 2006. ^b The source is a SNR candidate (G022.7583–0.4917) based on the Multi-Array Galactic Plane Imaging Survey (Helfand et al. 2006). ^c The source is a SNR candidate (G022.9917–0.3583) based on the Multi-Array Galactic Plane Imaging Survey (Helfand et al. 2006).

74.8 km s^{-1} (ID 6 in Table 3) is located in the south of SNR G22.7–0.2, in which the radio emission of the remnant shows a concave structure. A spectrophotometric distance of $4.2 \pm 0.4 \text{ kpc}$ was derived for the cluster GLIMPSE9 ($l=22^\circ 756$, $b=-0^\circ 400$) (Messineo et al. 2010) and of $\sim 4.6 \text{ kpc}$ for molecular complex (Messineo et al. 2014). The cluster is located in the concave structure (see the character “C” in Figure 6). Brunthaler et al. (2009) measured the distance of $4.59^{+0.38}_{-0.33} \text{ kpc}$ based on the trigonometric parallax for the massive star-forming region G23.01–0.41, which is near the H II region G023.029–0.405 (ID 12 in Table 3, $V_{\text{LSR}} \sim 76 \text{ km s}^{-1}$). Ellsworth-Bowers et al. (2013) presented a new distance estimation for dust-continuum-identified MC clumps, nine of which are probably associated with the 77 km s^{-1} GMCs (Table 2, Figure 8). Therefore, these objects are likely associated with the GMC with velocity $\sim 77 \text{ km s}^{-1}$ because of the systematic velocity coincidence.

As mentioned in Sections 3.2 and 4.1, we show that SNR G22.7–0.2 is interacting with the southern molecular gas in GMC G23.0–0.4W. The velocity coincidence of the H II region G022.760–0.485 and the ambient 77 km s^{-1} GMC indicates that the H II region is probably physically associated with SNR G22.7–0.2. The overlapping of the velocity dispersion of MCs and the radio emission in the concave structure (blue dotted line in Figure 6) strengthen above suggestion. The enhancement of the velocity dispersion in the concave structure (Figure 6) is probably due to the shock perturbation by SNR G22.7–0.2 and the H II region G022.760–0.485. Moreover, the interstellar extinction and spectral type of stars in the core of G022.760–0.485 and in the proximity of the southern border of SNR G22.7–0.2 supports the association of SNR G22.7–0.2 and G022.760–0.485 with the same GMC (Messineo et al. 2014). We note that a few of these radio-continuum sources may be composite sources (e.g., H II region G022.760–0.485). Helfand et al. (2006) identified G022.7583–0.4917 as a SNR candidate with diameter of $5'$ and Messineo et al. (2010) measured a radio spectral index of -0.98 of the source (see Region 3

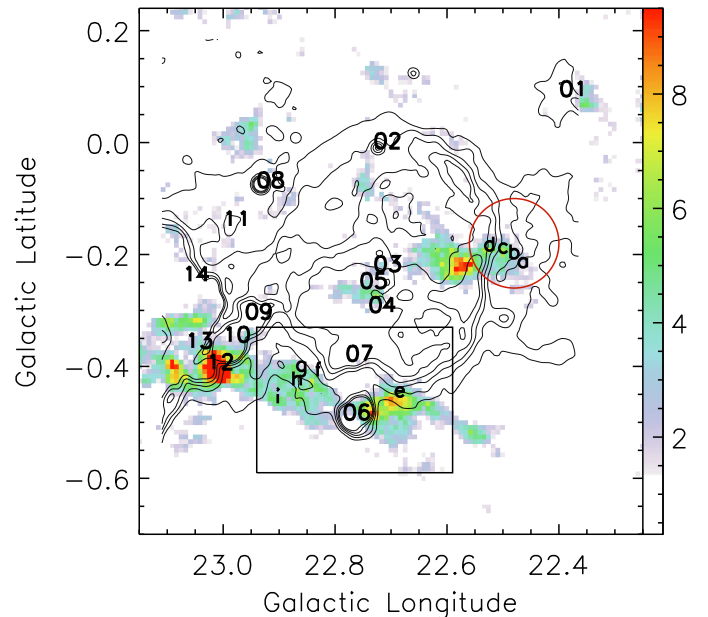


FIG. 8.— Location of the H II regions of SNR G22.7–0.2. The intensity map is the C^{18}O ($J=1-0$) emission in the interval of $70-81 \text{ km s}^{-1}$, overlaid with the VGPS 1.4 GHz radio continuum emission contours. The characters a–i indicate the dust-continuum-identified MC clumps in Table 2 and ID 01–14 indicate the H II regions listed in Table 3. The red circle shows the location of HESS J1832–093 (Laffon et al. 2013). The black box indicates the region of the shocked gas (see Figure 9).

in their Table 3).

Figure 9 shows a map intensity of the shocked gas in the south of the remnant. We find that the shocked gas is mainly located on the eastern edge of H II region G022.760–0.485. A part of the faint emission of the shocked gas also can be discerned in the northwestern boundary of the H II region. Nevertheless, there is little emission of the shocked gas in the region between the remnant and the H II region. A possible explanation is that the molecular gas in the north of H II region G022.760–0.485 were swept away by the SNR’s shock

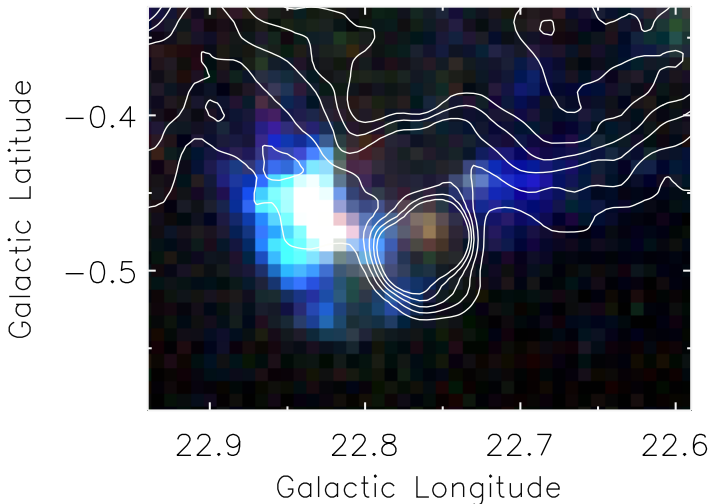


FIG. 9.— ^{12}CO ($J=1-0$) 3-color intensity map ($84-88\text{ km s}^{-1}$ in blue, $88-92\text{ km s}^{-1}$ in green, and $92-96\text{ km s}^{-1}$ in red) of SNR G22.7-0.2, which shows the distribution of the shocked gas in the south of the remnant. The map shows the southern border of SNR G22.7-0.2 and H II region G22.76-0.485.

and were exhausted by the interaction between the SNR and the H II region.

The age of the stellar cluster, which is located in the concave structure (see the character “C” in Figure 6), is about 27 to several Myrs (Messineo et al. 2010). On the other hand, the age of H II region G022.760-0.485, which is about $5'$ away from the stellar cluster, is about 0.1 to several Myrs (Dyson & Williams 1980). Meanwhile, Messineo et al. (2014) estimated the age of the O-types stars associated with GMC G23.0-0.4 (the GMC G23.3-0.3 in their paper) of a likely age of 5-8 Myr. Interestingly, one of star (ID 25 in their paper) is exactly located on the center of the H II region G022.760-0.485. Presuming that the stellar cluster and H II region G022.760-0.485 were birthed in the same MCs in the southern edge of the remnant, the progenitor’s activities of SNR G22.7-0.2 seem a plausible triggering mechanism for the new generation of star formation in the ambient GMC.

4.3. The Very High-Energy γ -ray Source HESS J1832-093 Adjacent to the Remnant

The MCs that SNRs are associated or interacting with are a good probe for the hadronic process (see the recent view in Chen et al. 2014). Several SNRs are detected with bright high-energy emission by their interaction with nearby MCs, e.g., SNRs W28 (Aharonian et al. 2008) and IC 443 (Abdo et al. 2010; Ackermann et al. 2013; Su et al. 2014). At the west boundary of SNR G22.7-0.2, HESS J1832-093 is detected with a significance of 5.6σ (Laffon et al. 2013). Laffon et al. (2013) found an infrared source, 2MASS J18324516-0921545, around the position of a point-like X-ray source, XMMU J183245-0921539. They discussed the possible origination of the VHE source. The VHE emission is spatially coincident with the $1 \times 10^5 M_{\odot}$ GMC G22.6-0.2 (Figures 1 and 8). A possible origin of the γ -rays is hadronic interactions of the cosmic rays with the GMC.

There is no VHE emission detected in the south of SNR G22.7-0.2, where massive molecular gas in GMC G23.0-0.4W is located. However, Frail et al. (2013) argued that the correlation between the VHE γ -ray source HESS J1834-087 and the 1720 MHz OH masers of SNR W41 favors a hadronic interpretation for the VHE emission. The 74 km s^{-1} radial velocity of the OH masers is consistent with the velocity of GMC G23.0-0.4, indicating that SNR W41, behind the GMC, is in physical contact with it (Frail et al. 2013). Abramowski et al. (2014) discussed the origin of the high-energy emission of SNR W41 in detail and they also favored the hadronic scenario from GeV to TeV extended emission. Why is there no detectable high-energy emission in the south of SNR G22.7-0.2? Further searches for detecting and characterizing high-energy emission in the vicinity of SNR G22.7-0.2 are needed to be performed.

5. SUMMARY

Millimeter and submillimeter CO studies have been performed on SNR G22.7-0.2. We conclude the main results of our analysis as follows.

1. We have found spatial and kinematic evidence to support the association between SNR G22.7-0.2 and the nearby 77 km s^{-1} MCs. The intensity map of the molecular gas in GMC G23.0-0.4W in $75-79\text{ km s}^{-1}$ displays filamentary structures surrounding the southern boundary of the remnant. The molecular gas ($l=22^{\circ}833, b=-0^{\circ}467$) shows a redshifted broadening ($77-110\text{ km s}^{-1}$) in the ^{12}CO ($J=1-0$ and $J=2-1$) line emission, which indicates convincing kinematic evidence for SNR-MC interaction.

2. We place SNR G22.7-0.2 at a kinematic distance of $4.4 \pm 0.4\text{ kpc}$ based on the association between the remnant and the 77 km s^{-1} GMC G23.0-0.4. The SNR is located at the near side of the Scutum-Crux arm, where several H II regions are evolving in the complicated MC environment.

3. We suggest that the overlapping H II region G022.760-0.485 with a radial velocity $\sim 74.8\text{ km s}^{-1}$ is possibly associated with SNR G22.7-0.2 and is likely to be triggered by the stellar winds from the massive progenitor of the remnant.

4. SNRs G22.7-0.2 and W41 are both interacting with $V_{\text{LSR}} \sim 77\text{ km s}^{-1}$ GMC G23.0-0.4, indicating that they very likely have a similar distance.

The authors acknowledge the staff members of the Qinghai Radio Observing Station at Delingha for their support of the observations. We thank the anonymous referee for valuable advice and comments. This work is supported by NSFC grants 11103082, 11233001, 11233007, and 10725312. Y.S. acknowledges support from grant BK2011889. The work is a part of the Multi-Line Galactic Plane Survey in CO and its Isotopic Transitions, also called the Milky Way Imaging Scroll Painting, which is supported by the Strategic Priority Research Program, the Emergence of Cosmological Structures of the Chinese Academy of Sciences, grant No. XDB09000000.

REFERENCES

- Abdo, A. A., Ackermann, M., Ajello, M., et al. 2010, *ApJ*, 712, 459
- Abramowski, A., Aharonian, F., Ait Benkhali, F., et al. 2014, *A&A*, in press (arXiv:1407.0862)
- Ackermann, M., Ajello, M., Allafort, A., et al. 2013, *Science*, 339, 807
- Aharonian, F., Akhperjanian, A. G., Bazer-Bachi, A. R., et al. 2008, *A&A*, 481, 401
- Albert, J., Aliu, E., Anderhub, H., et al. 2006, *ApJ*, 643, L53
- Anderson, L. D., Bania, T. M., Balsaer, D. S., et al. 2014, *ApJS*, 212, 1
- Anderson, L. D., Bania, T. M., Balsaer, D. S., & Rood, R. T. 2011, *ApJS*, 194, 32
- Brunthaler, A., Reid, M. J., Menten, K. M., et al. 2009, *ApJ*, 693, 424
- Chen, Y., Jiang, B., Zhou, P., et al. 2014, in *IAU Symposium*, Vol. 296, *Supernova Environmental Impacts*, ed. A. Ray & R. A. McCray, 170–177
- Dame, T. M., Elmegreen, B. G., Cohen, R. S., & Thaddeus, P. 1986, *ApJ*, 305, 892
- Dame, T. M., Hartmann, D., & Thaddeus, P. 2001, *ApJ*, 547, 792
- Dyson, J. E., & Williams, D. A. 1980, *Physics of the interstellar medium* (New York: Halsted Press), 204
- Ellsworth-Bowers, T. P., Glenn, J., Rosolowsky, E., et al. 2013, *ApJ*, 770, 39
- Frail, D. A., Claussen, M. J., & Méhault, J. 2013, *ApJ*, 773, L19
- Frerking, M. A., Langer, W. D., & Wilson, R. W. 1982, *ApJ*, 262, 590
- Green, D. A. 1991, *PASP*, 103, 209
- Helfand, D. J., Becker, R. H., White, R. L., Fallon, A., & Tuttle, S. 2006, *AJ*, 131, 2525
- Herbst, E., & Leung, C. M. 1989, *ApJS*, 69, 271
- Laffon, H., Acero, F., Brun, F., et al. 2013, arXiv:1308.0475
- Leahy, D. A., & Tian, W. W. 2008, *AJ*, 135, 167
- Lockman, F. J. 1989, *ApJS*, 71, 469
- Lockman, F. J., Pisano, D. J., & Howard, G. J. 1996, *ApJ*, 472, 173
- Messineo, M., Figer, D. F., Davies, B., et al. 2010, *ApJ*, 708, 1241
- Messineo, M., Menten, K. M., Figer, D. F., et al. 2014, *A&A*, 569, A20
- Milam, S. N., Savage, C., Brewster, M. A., Ziurys, L. M., & Wyckoff, S. 2005, *ApJ*, 634, 1126
- Reach, W. T., Rho, J., Tappe, A., et al. 2006, *AJ*, 131, 1479
- Reid, M. J., Menten, K. M., Brunthaler, A., et al. 2014, *ApJ*, 783, 130
- Roman-Duval, J., Jackson, J. M., Heyer, M., et al. 2009, *ApJ*, 699, 1153
- Seta, M., Hasegawa, T., Sakamoto, S., et al. 2004, *AJ*, 127, 1098
- Sewilo, M., Watson, C., Araya, E., et al. 2004, *ApJS*, 154, 553
- Shan, W. L., Yang, J., Shi, S. C., et al. 2012, *IEEE Transactions on Terahertz Science and Technology*, 2, 593
- Snell, R. L., Hollenbach, D., Howe, J. E., et al. 2005, *ApJ*, 620, 758
- Snell, R. L., Scoville, N. Z., Sanders, D. B., & Erickson, N. R. 1984, *ApJ*, 284, 176
- Stil, J. M., Taylor, A. R., Dickey, J. M., et al. 2006, *AJ*, 132, 1158
- Su, Y., Chen, Y., Yang, J., et al. 2009, *ApJ*, 694, 376
- . 2011, *ApJ*, 727, 43
- Su, Y., Fang, M., Yang, J., Zhou, P., & Chen, Y. 2014, *ApJ*, 788, 122
- Taylor, J. H., & Cordes, J. M. 1993, *ApJ*, 411, 674
- Thompson, M. A., Hatchell, J., Walsh, A. J., MacDonald, G. H., & Millar, T. J. 2006, *A&A*, 453, 1003
- Zhang, Z., Gao, Y., & Wang, J. 2010, *Science China Physics, Mechanics, and Astronomy*, 53, 1357
- Zuo, Y. X., Li, Y., Sun, J. X., et al. 2011, *Acta Astronomica Sinica*, 52, 152